

# FCVSR: A Frequency-aware Method for Compressed Video Super-Resolution

Qiang Zhu, Fan Zhang, *Member, IEEE*, Feiyu Chen, *Member, IEEE*,  
Shuyuan Zhu, *Member, IEEE*, David Bull, *Fellow, IEEE*, and Bing Zeng, *Fellow, IEEE*

**Abstract**—Compressed video super-resolution (SR) aims to generate high-resolution (HR) videos from the corresponding low-resolution (LR) compressed videos. Recently, some compressed video SR methods attempt to exploit the spatio-temporal information in the frequency domain, showing great promise in super-resolution performance. However, these methods do not differentiate various frequency subbands spatially or capture the temporal dynamics, potentially leading to sub-optimal results. In this paper, we propose a deep frequency-based compressed video SR model (FCVSR) consisting of a motion-guided adaptive alignment (MGAA) network and a multi-frequency feature refinement (MFFR) module. Additionally, a frequency-aware contrastive loss is proposed for training FCVSR, in order to reconstruct finer spatial details. The proposed model has been evaluated on three public compressed video super-resolution datasets, with results demonstrating its effectiveness when compared to existing works in terms of super-resolution performance (up to a 0.14dB gain in PSNR over the second-best model) and complexity.

**Index Terms**—video super-resolution, video compression, frequency, contrastive learning, deep learning, FCVSR.

## I. INTRODUCTION

IN recent years, video super-resolution (VSR) has become a popular research topic in image and video processing. It typically takes a low-resolution (LR) video clip and reconstructs its corresponding high-resolution (HR) counterpart with improved perceptual quality. VSR has been used for various application scenarios including video surveillance [1, 2], medical imaging [3, 4] and video compression [5, 6]. Inspired by the latest advances in deep learning, existing VSR methods leverage various deep neural networks [7–12] in model design, with notable examples including BasicVSR [13] and TCNet [14] based on optical flow [7, 8], TDAN [15] and EDVR [16] based on deformable convolution networks (DCN) [9, 10], TTVSR [17] and FTVSR++ [18] based on vision transformers [11], and Upscale-A-Video [19] and MGLD-VSR [20] based on diffusion models [12].

When VSR is applied to video compression, it shows great potential in producing significant coding gains when integrated with conventional [21, 22] and learning-based video codecs [23, 24]. In these cases, in addition to the quality degradation induced by spatial down-sampling, video compression

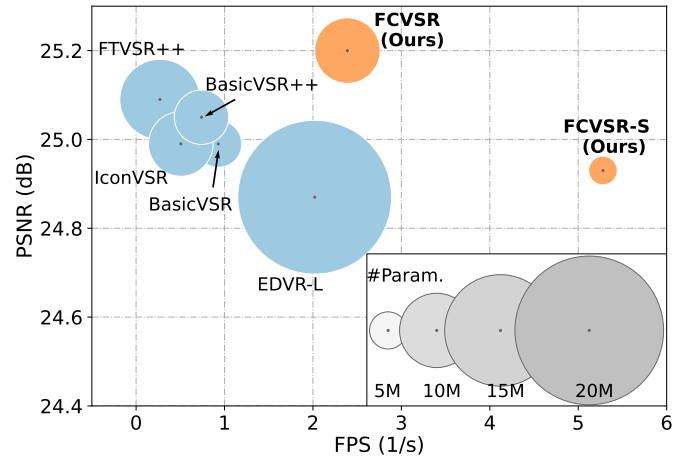


Fig. 1. Illustration of performance-complexity trade-offs for different compressed VSR models. It can be observed that the proposed FCVSR model offers better super-resolution performance with lower complexity compared to benchmark methods.

also generates compression artifacts within low-resolution content [25], which makes the super-resolution task more challenging. Previous works reported that general VSR methods may not be suitable for dealing with both compression [26–28] and down-sampling degradations [13, 16], so bespoke compressed video super-resolution methods [18, 29–37] have been proposed to address this issue. Among these methods, there is a class of compressed VSR models [18, 29, 37] focuses on performing super-resolution in the frequency domain, such as COMISR [29], FTVSR [37] and FTVSR++ [18], which align well with the nature of super-resolution, recovering the lost high-frequency details in the low-resolution content. However, it should be noted that these methods do not differentiate various frequency subbands spatially or capture the temporal frequency dynamics. This limits the reconstruction of spatial details and the accuracy of temporal alignment, resulting in suboptimal super-resolution performance.

In this context, this paper proposes a novel deep Frequency-aware Compressed VSR model, **FCVSR**, which exploits both spatial and temporal information in the frequency domain. It employs a new motion-guided adaptive alignment (MGAA) module that estimates multiple motion offsets between frames in the frequency domain, based on which cascaded adaptive convolutions are performed for feature alignment. We also designed a multi-frequency feature refinement (MFFR) module based on a decomposition-enhancement-aggregation strategy to restore high-frequency details within high-resolution videos.

Q. Zhu, F. Chen, S. Zhu, and B. Zeng are with the School of Information and Communication Engineering, University of Electronic Science and Technology of China, Chengdu, China (e-mail: eezsy@uestc.edu.cn).

Q. Zhu is also with the School of Computer Science, University of Bristol, Bristol, United Kingdom.

F. Zhang and D. Bull are with the School of Computer Science, University of Bristol, Bristol, United Kingdom.

To optimize the proposed FCVSR model, we have developed a frequency-aware contrastive (FC) loss for recovering high-frequency fine details. The main contributions of this work are summarized as follows:

- 1) A new **motion-guided adaptive alignment (MGAA)** module, which achieves improved feature alignment through explicitly considering the motion relationship in the frequency domain. To our knowledge, it is the first time that this type of approach is employed for video super-resolution. Compared to commonly used deformable convolution-based alignment modules [15, 16, 38] in existing solutions, MGAA offers better flexibility, higher performance, and lower complexity.
- 2) A novel **multi-frequency feature refinement (MFFR)** module, which provides the capability to recover fine details by using a decomposition-enhancement-aggregation strategy. Unlike existing frequency-based refinement models [39, 40] that do not decompose features into multiple frequency subbands, our MFFR module explicitly differentiates features of different subbands, gradually performing the enhancement of subband features.
- 3) A **frequency-aware contrastive (FC)** loss is employed using contrastive learning based on the divided high-/low-frequency groups, supervising the reconstruction of finer spatial details.

Based on a comprehensive experiment, the proposed FCVSR model has demonstrated its superior performance in both quantitative and qualitative evaluations on three public datasets, when compared to five existing compressed VSR methods, with up to a 0.14dB PSNR gain. Moreover, it is also associated with relatively low computational complexity, which offers an excellent trade-off for practical applications (as shown in Fig. 1).

## II. RELATED WORK

This section reviews existing works in the research areas of video super-resolution (VSR), in particular focusing on compressed VSR and frequency-based VSR which are relevant to the nature of this work. We have also briefly summarized the loss functions typically used for VSR.

### A. Video Super-Resolution

VSR is a popular low-level vision task that aims to construct an HR video from its LR counterpart. State-of-the-art VSR methods [13–17, 38, 41–43] typically leverage various deep neural networks [7–12, 15], achieving significantly improved performance compared to conventional super-resolution methods based on classic signal processing theories [44, 45]. For example, BasicVSR [13], IconVSR [13] and TCNet [14] utilize optical flow [7, 8] networks to explore the temporal information between neighboring frames in order to achieve temporal feature alignment. Deformable convolution-based alignment methods [15, 16] have also been proposed based on the DCN [9, 10], with typical examples such as TDAN [15] and EDVR [16]. DCN has been reported to offer better capability in modeling geometric transformations between frames, resulting in more accurate motion estimation results. More

recently, several VSR models [38, 46, 47] have been designed with a flow-guided deformable alignment (FGDA) module that combines optical flow and DCN to achieve improved temporal alignment, among which BasicVSR++ [38] is a commonly known example. Moreover, more advanced network structures have been employed for VSR, such as Vision Transformer (ViT) and diffusion models. TTVSR [17] is a notable ViT-based VSR method, which learns visual tokens along spatio-temporal trajectories for modeling long-range features. CTVSR [48] further exploits the strengths of Transformer-based and recurrent-based models by concurrently integrating the spatial information derived from multi-scale features and the temporal information acquired from temporal trajectories. Furthermore, diffusion models [12, 49] have been utilized [19, 20, 50] to improve the perceptual quality of super-resolved content. Examples include Upscale-A-Video [19] based on a text-guided latent diffusion framework and MGLD-VSR [20] that exploits the temporal dynamics based on diffusion model within LR videos.

Recently, some VSR methods [18, 37, 40, 51] are designed to perform low-resolution video up-sampling in the **frequency** domain rather than in the spatial domain. For example, FTVSR++ [18] has been proposed to use a degradation-robust frequency-Transformer to explore the long-range information in the frequency domain; similarly, a multi-frequency representation enhancement with privilege information (MFPI) network [40] has been developed with a spatial-frequency representation enhancement branch that captures the long-range dependency in the spatial dimension, and an energy frequency representation enhancement branch to obtain the inter-channel feature relationship; DFVSR [51] applies the discrete wavelet transform to generate directional frequency features from LR frames and achieve directional frequency-enhanced alignment. Further examples include COMISR [29] which applies a Laplacian enhancement module to generate high-frequency information for enhancing fine details, GAVSR [36] that employs a high-frequency mask based on Gaussian blur to assist the attention mechanism and FTVSR [37] which is based on a Frequency-Transformer to conduct self-attention over a joint space-time-frequency domain. However, these frequency-based methods do not fully explore the multiple frequency subbands of the features or account for the motion relationships in the frequency domain, which restricts the exploration of more valuable information.

In many application scenarios, VSR is applied to compressed LR content, making the task even more challenging compared to uncompressed VSR. Recently, this has become a specific research focus, and numerous **compressed VSR** methods [18, 29–36] have been developed based on coding priors. For example, CD-VSR [30] utilizes motion vectors, predicted frames, and prediction residuals to reduce compression artifacts and obtain spatio-temporal details for HR content; CIAF [31] employs recurrent models together with motion vectors to characterize the temporal relationship between adjacent frames; CAVSR [32] also adopts motion vectors and residual frames to achieve information fusion. It is noted that these methods are typically associated with increased complexity in order to fully leverage these coding

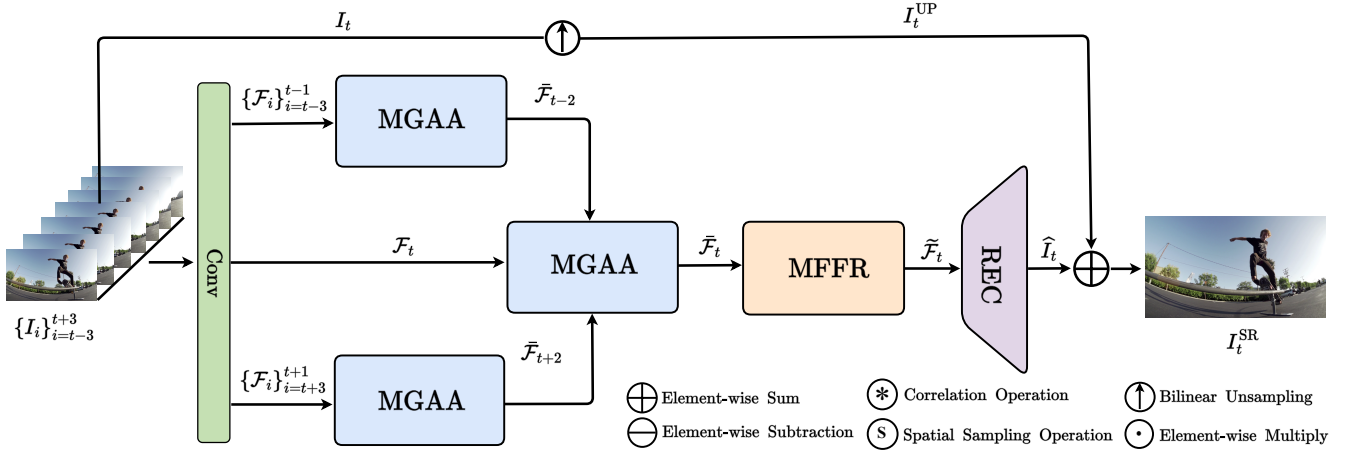


Fig. 2. The architecture of FCVSR model. An LR compressed video is fed into a convolution layer, MGAA, MFFR, and reconstruction (REC) modules to generate an HR video.

priors, which limits their adoption in practical applications.

### B. Loss Functions of Video Super-Resolution

When VSR models were optimized, various loss functions were employed to address different application scenarios. These can be classified into two primary groups: spatial- and frequency-based. Spatial-based loss functions aim to minimize the pixel-wise discrepancy between the generated HR frames and the corresponding ground truth (GT) frames during training, with  $L_1$  and  $L_2$  losses are the commonly used objectives. Furthermore, the Charbonnier loss [52] is a differentiable and smooth approximation of the  $L_2$  loss, with similar robustness as the  $L_1$  loss for reducing the weight of large errors and focusing more on smaller errors. Recently, some frequency-based loss functions [40, 53, 54] are proposed to explore the high-frequency information. For example, a Fourier space loss [53] calculated the frequency components in the Fourier domain for direct emphasis on the frequency content for restoration of high-frequency components. A focal frequency loss [54] generated the frequency representations using the discrete Fourier transform to supervise the generation of high-frequency information. However, these frequency-based loss functions typically observe global frequency information without decomposing features into different frequency subbands, which constrains VSR models to recover fine details.

## III. PROPOSED METHOD

To address the issues associated with existing video super-resolution (VSR) methods, this paper proposes a novel frequency-aware VSR model, FCVSR, specifically for compressed content, targeting improved trade-off between performance and complexity. As illustrated in Fig. 2, for the current LR video frame  $I_t$ , FCVSR takes seven LR video frames  $\{I_i\}_{i=t-3}^{t+3}$  as input and produces an HR video frame  $I_t^{\text{SR}}$ , targeting the uncompressed HR counterpart  $I_t^{\text{HR}}$  of  $I_t$ .

Specifically, each input frame is fed into a convolution layer with a  $3 \times 3$  kernel size,

$$\mathcal{F}_i = \text{Conv}(I_i) \in \mathbb{R}^{h \times w \times c}, i = t-3, \dots, t+3 \quad (1)$$

where  $h, w, c$  are the height, width, and channel of feature.

In order to achieve pixel-level alignment between the current frame and other input neighboring frames, multiple motion-guided adaptive alignment (MGAA) modules are employed, which takes 3 sets of features generated by the convolution layer as input and outputs a single set of features. First, this is applied to the features corresponding to the first three frames,  $\{\mathcal{F}_i\}_{i=t-3}^{t-1}$ , and produces  $\bar{\mathcal{F}}_{t-2}$ . This operation is repeated for  $\{\mathcal{F}_i\}_{i=t+1}^{t+3}$  to obtain  $\bar{\mathcal{F}}_{t+2}$ .  $\bar{\mathcal{F}}_{t-2}$ ,  $\mathcal{F}_t$  and  $\bar{\mathcal{F}}_{t+2}$  are then fed into the MGAA module again to generate the final aligned feature set  $\bar{\mathcal{F}}_t$ .

Following alignment operation, the aligned feature  $\bar{\mathcal{F}}_t$  is processed by into a multi-frequency feature refinement (MFFR) module to obtain the refined feature  $\tilde{\mathcal{F}}_t$ , before input into a reconstruction (REC) module, which outputs the HR residual frame  $\hat{I}_t$ . Finally, this is combined with the bilinear up-sampled compressed frame  $I_t^{\text{UP}}$  (from  $I_t$ ) through element-wise sum to obtain the final HR frame  $I_t^{\text{SR}}$ .

### A. Motion-Guided Adaptive Alignment

Most existing VSR methods estimate a single optical flow [8, 55, 56] or offset [15, 16] between frames only once to achieve feature alignment, which limits the accuracy of feature alignment in some cases. In addition, existing optical flow-based alignment modules [13, 14, 57] or deformable convolution-based alignment modules [15, 16] are typically associated with high complexity, restricting their adoption in practical applications. To address these problems, we developed a motion-guided adaptive alignment (MGAA) module that estimates different types of motion between frames, which are further used for feature alignment through adaptive convolutions. An MGAA module, as illustrated in Fig. 3, consists of a Motion Estimator, Kernel Predictor, and a motion-guided adaptive convolution (MGAC) layer in a bidirectional propagation manner.

Specifically, without loss of generality, when the MGAA module takes the set of features  $\{\mathcal{F}_i\}_{i=t-3}^{t-1}$  as input (shown in Fig. 3), these features are first divided into the forward set

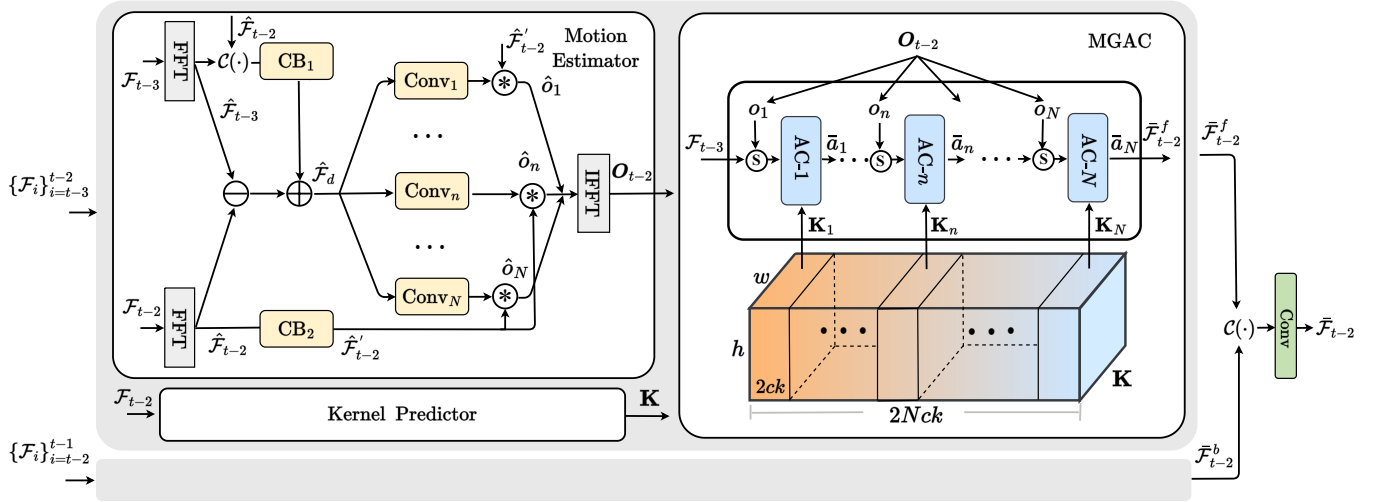


Fig. 3. The architecture of motion-guided adaptive alignment (MGAA) module. The set of features  $\{\mathcal{F}_i\}_{i=t-3}^{t-1}$  are divided into the forward set  $\{\mathcal{F}_i\}_{i=t-3}^{t-2}$  and the backward set  $\{\mathcal{F}_i\}_{i=t-2}^{t-1}$  for feature alignment.

$\{\mathcal{F}_i\}_{i=t-3}^{t-2}$  and the backward set  $\{\mathcal{F}_i\}_{i=t-2}^{t-1}$  for bidirectional propagation in the MGAA module. The forward features  $\{\mathcal{F}_i\}_{i=t-3}^{t-2}$  are then fed into the Motion Estimator  $\text{ME}(\cdot)$  to perform motion prediction, resulting in motion offsets  $\mathbf{O}_{t-2}$ :

$$\mathbf{O}_{t-2} = \{o_n\}_{n=1}^N = \text{ME}(\mathcal{F}_{t-2}, \mathcal{F}_{t-3}), o_n \in \mathbb{R}^{h \times w \times 2}, \quad (2)$$

where  $N$  is the number of motion offsets.

The feature  $\mathcal{F}_{t-2}$  is also input into the Kernel Predictor  $\text{KP}(\cdot)$  to generate  $N$  adaptive convolution kernels:

$$\mathbf{K} = \{\mathbf{K}_n\} = \text{KP}(\mathcal{F}_{t-2}), \mathbf{K}_n \in \mathbb{R}^{h \times w \times 2ck}, \quad (3)$$

where  $k$  is the kernel size of the adaptive convolution.

Based on the motion offsets and kernel sets, the feature  $\mathcal{F}_{t-3}$  is processed by the MGAC layer  $\text{MGAC}(\cdot)$  to achieve the feature alignment (with  $\mathcal{F}_{t-2}$ ):

$$\bar{\mathcal{F}}_{t-2}^f = \text{MGAC}(\mathcal{F}_{t-3}, \mathbf{O}_{t-2}). \quad (4)$$

In parallel, the same operation is performed for the backward set to obtain the aligned features  $\bar{\mathcal{F}}_{t-2}^b$ . Finally,  $\bar{\mathcal{F}}_{t-2}^f$  and  $\bar{\mathcal{F}}_{t-2}^b$  are concatenated and fed into a convolution layer to obtain the final aligned feature  $\bar{\mathcal{F}}_{t-2}$ .

1) *Motion Estimator*: The Motion Estimator is applied in the frequency domain by performing the Fast Fourier Transform (FFT) on the input feature sets, and the resulting frequency features are denoted as  $\hat{\mathcal{F}}_{t-2}$  and  $\hat{\mathcal{F}}_{t-3}$  corresponding to  $\mathcal{F}_{t-2}$  and  $\mathcal{F}_{t-3}$  respectively. The difference between these frequency features are then combined with their concatenated version (through a convolution block  $\text{CB}_1$ ), obtaining the difference feature  $\hat{\mathcal{F}}_d$ :

$$\hat{\mathcal{F}}_d = \hat{\mathcal{F}}_{t-2} - \hat{\mathcal{F}}_{t-3} + \text{CB}_1(\mathcal{C}(\hat{\mathcal{F}}_{t-2}, \hat{\mathcal{F}}_{t-3})), \quad (5)$$

where  $\text{CB}_1$  is a convolution block consisting of a  $3 \times 3$  convolution layer with  $2c$  channels, a ReLU activation function followed a  $3 \times 3$  convolution layer with  $c$  channels.  $\mathcal{C}(\cdot)$  represents the concatenation operation.

The difference feature  $\hat{\mathcal{F}}_d$  is then input into multiple branches with different kernel sizes to learn motion sets,  $\{\hat{o}_n\}$

in the frequency domain. For the  $n$ -th branch, the motion offset is calculated as follows:

$$\hat{o}_n = \text{Conv}_n(\hat{\mathcal{F}}_d) \circledast \text{CB}_2(\hat{\mathcal{F}}_{t-2}), \quad (6)$$

where  $\text{Conv}_n$  consists of two convolution layers with kernel size  $2n + 1$ , a PReLU activation function, and channel attention [58].  $\circledast$  is a correlation operation to obtain the correlation between features.  $\text{CB}_2$  is a convolution block consisting of a  $3 \times 3$  convolution layer with  $c$  channels, a ReLU activation function and a  $3 \times 3$  convolution layer with 2 channels.

The learned multiple frequency motion offsets are transformed into the spatial domain by inverse FFT, resulting in the motion offsets  $\{o_n\}$ .

2) *Kernel Predictor*: To predict adaptive convolution kernels, we designed a Kernel Predictor  $\text{KP}(\cdot)$  (formulated by Eq. (3)), which consists of a  $3 \times 3$  convolution layer and  $1 \times 1$  convolution layer to generate two directional kernels. The kernel set  $\mathbf{K}$  predicted here is a  $2Nck$ -dim vector representing  $N$  sets of kernels  $\{\mathbf{K}_n\}_{n=1}^N$ . For the  $n$ -th predicted kernel  $\mathbf{K}_n$ , it has two 1-dim kernels  $\mathcal{K}_n^v$  and  $\mathcal{K}_n^h$  with sizes  $k \times 1$  and  $1 \times k$  and  $c$  channels.

3) *Motion-Guided Adaptive Convolution Layer*: We utilize the estimated multiple motion offsets to independently guide the feature spatial sampling for each adaptive convolution in the MGAC layer based on predicted kernels. As shown in Fig. 3, at the  $n$ -th adaptive convolution operation,  $\text{AC-}n$ , the aligned feature  $\bar{a}_n$  is calculated as:

$$\bar{a}_n = \text{AC-}n(\bar{a}_{n-1}, o_n, \mathbf{K}_n) = \mathbb{S}(\bar{a}_{n-1}, o_n) * \mathcal{K}_n^h * \mathcal{K}_n^v, \quad (7)$$

where  $n = 1, \dots, N$ ,  $\bar{a}_0 = \mathcal{F}_{t-3}$ ,  $\bar{a}_N = \bar{\mathcal{F}}_{t-2}$ ,  $\mathbb{S}(\cdot, \cdot)$  represents the spatial sampling operation and  $*$  is the channel-wise convolution operator that performs convolutions in a spatially-adaptive manner.

## B. Multi-Frequency Feature Refinement

In this work, rather than restoring high-frequency information within the entire frequency range as existing works [40,

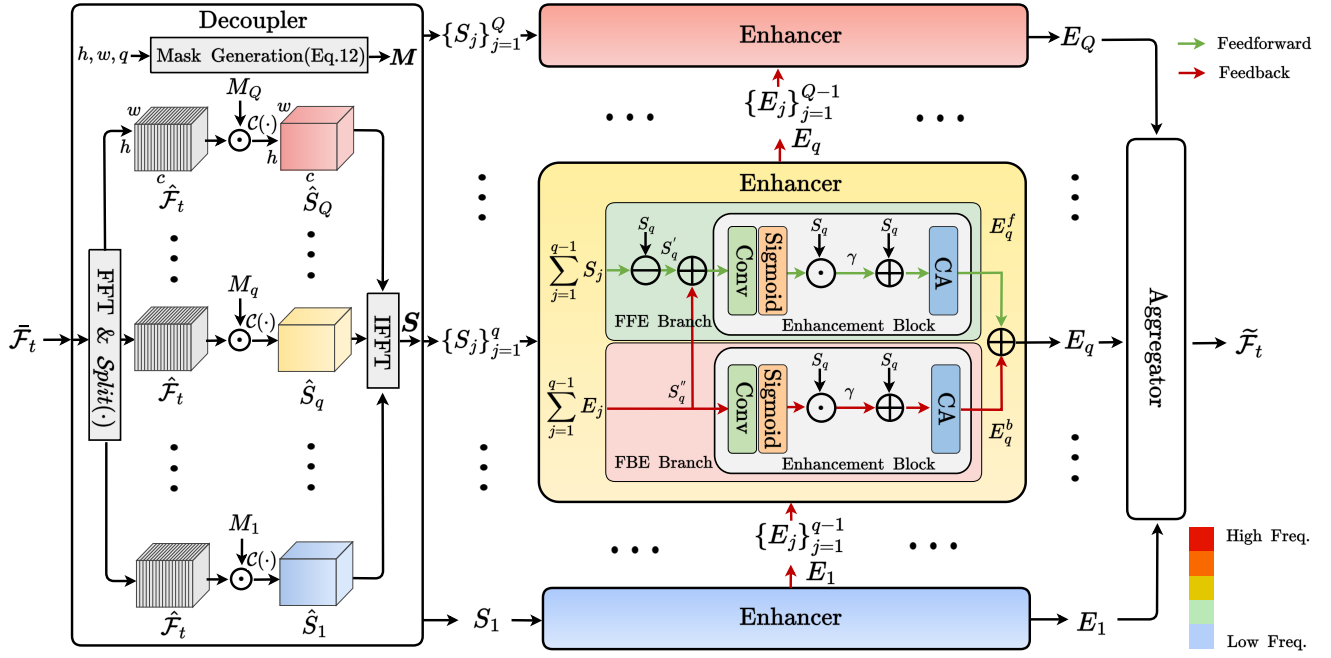


Fig. 4. The architecture of multi-frequency feature refinement (MFFR) module.

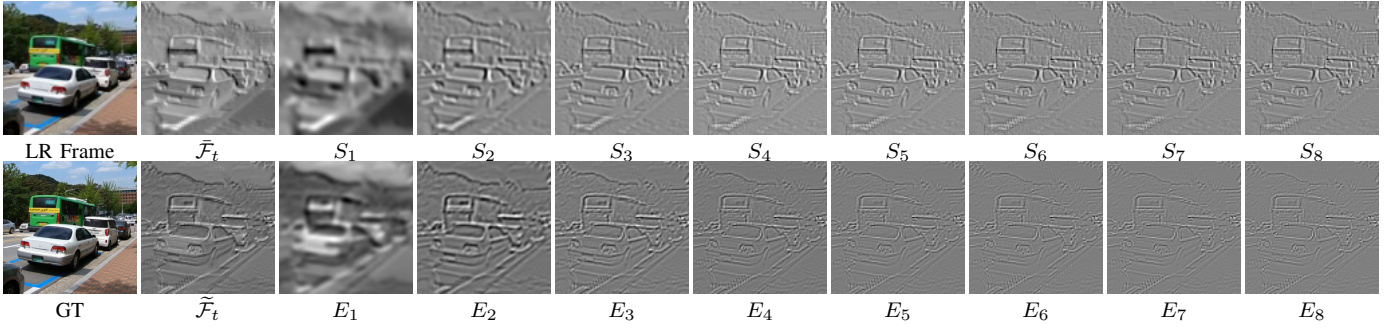


Fig. 5. Visualization of input feature, output feature, decoupled features, enhanced features in the MFFR module.

51], we designed a multi-frequency feature refinement (MFFR) module to refine the input feature in different frequency subbands, as shown in Fig. 4. It consists of *Decoupler*, *Enhancer*, and *Aggregator* modules, based on the decomposition-enhancement-aggregation strategy.

Specifically, the *Decoupler* module employs Gaussian band-pass filters to decompose the input feature  $\tilde{F}_t \in \mathbb{R}^{h \times w \times c}$  into  $Q$  features:

$$\mathbf{S} = \{S_j\}_{j=1}^Q = \text{Decoupler}(\tilde{F}_t). \quad (8)$$

The decomposed feature set  $\mathbf{S}$  (or its subsets) is then fed into multiple *Enhancer* modules to obtain the enhanced features  $\mathbf{E} = \{E_j\}_{j=1}^Q$ . Specifically, for the  $q^{\text{th}}$  subband, the subset  $\{S_j\}_{j=1}^q$ , and enhanced features  $\{E_j\}_{j=1}^{q-1}$  for the lower subbands (if applicable) are input into the *Enhancer* module to obtain the enhanced feature  $E_q$  at this subband level. This process is described by:

$$E_q = \begin{cases} \text{Enhancer}(S_1), q = 1, \\ \text{Enhancer}(\{S_j\}_{j=1}^q, \{E_j\}_{j=1}^{q-1}), q = 2, \dots, Q. \end{cases} \quad (9)$$

For the lowest subband, we additionally apply a mean filter on  $S_1$  before inputting it into *Enhancer*.

Finally, the *Aggregator* module is employed to aggregate the enhanced features  $\mathbf{E}$  and obtain the refined feature:

$$\tilde{F}_t = \text{Aggregator}(\mathbf{E}). \quad (10)$$

1) *Decoupler*: The workflow of the *Decoupler* module is illustrated in Fig. 4. To decompose the input feature  $\tilde{F}_t$  into different frequency subbands, the input feature is first transformed to the frequency domain by FFT. The resulting frequency feature  $\hat{F}_t \in \mathbb{R}^{h \times w \times c}$  is then split along the channel dimension by *Split*( $\cdot$ ) operation to obtain  $c$  frequency channel features. Sequentially, the *Decoupler* module generates  $Q$  Gaussian band-pass filter masks  $\mathbf{M} = \{M_j\}_{j=1}^Q$ ,  $M_j \in \mathbb{R}^{h \times w \times 1}$ . For each  $M_j$ , its truncation frequency  $d_j$  is calculated based on the width  $h$  and height  $w$  of the input feature:

$$d_j = \frac{j \sqrt{(\frac{h}{2})^2 + (\frac{w}{2})^2}}{Q}, \quad (11)$$

and  $M_j$  is given by:

$$M_j(u, v) = \exp\left(\frac{-[(u-h/2)^2 + (v-w/2)^2]}{2d_j^2}\right) - \sum_{l=1}^{j-1} \exp\left(\frac{-[(u-h/2)^2 + (v-w/2)^2]}{2d_l^2}\right). \quad (12)$$

The frequency channel features are multiplied by each of these band-pass filter masks and then concatenated to obtain the decomposed frequency feature  $\hat{S}_q$ . Finally, feature  $\hat{S}_q$  is transformed to the spatial domain through inverse FFT, producing the corresponding decomposed feature  $S_q$ .

2) *Enhancer*: To enhance the decomposed frequency feature  $S$  within each subband, the corresponding subset of  $S$ ,  $\{S_j\}_{j=1}^q$ , and the enhanced feature set  $\{E_j\}_{j=1}^{q-1}$  from the lower subband are fed into the *Enhancer* module for feature enhancement. The *Enhancer* module consists of a feedforward enhancement (FFE) branch and a feedback enhancement (FBE) branch, both contain an enhancement block. As show in Fig. 4, in the FFE branch, the input feature subset,  $\{S_j\}_{j=1}^q$ , is summed together, and subtracted by the decomposed feature  $S_q$  to obtain a high-frequency feature  $S'_q$ . The enhanced feature set  $\{E_j\}_{j=1}^{q-1}$  is summed together in the FBE branch, obtaining another high-frequency feature  $S''_q$ . The sum of  $S'_q$  and  $S''_q$  is then input into the enhancement block, which consists of a  $3 \times 3$  convolution layer Conv, a sigmoid activation function  $\sigma$  and a channel attention (CA) [58], to obtain the feedforward enhanced feature  $E_q^f$ .

In the FBE branch,  $S''_q$  is also processed by the enhancement block to obtain the feedback enhanced feature  $E_q^b$ , which will then be combined with  $E_q^f$  to produce the final enhanced feature  $E_q$ . It is noted that when  $q = 1$  (corresponding to the lowest subband), we additionally apply a mean filter on  $S_q$  which replaces  $\{S_j\}_{j=1}^q$  as the input of the *Enhancer* module and there is no FBE branch here.

3) *Aggregator*: To aggregate the enhanced frequency feature in each subband, we use the following equation to sum them together before applying a channel attention (CA) to strengthen the interaction between feature channels:

$$\tilde{F}_t = \text{CA}\left(\sum_{j=1}^Q E_j\right). \quad (13)$$

Figure 5 provides a visualization of the intermediate results generated in the MFFR module. It can be observed that the resulting features at each stage exhibit the characteristics expected in the design - features corresponding to high-frequency subbands contain finer details, and vice versa.

### C. Reconstruction Module

To generate an HR video from the refined feature  $\tilde{F}_t$ , the scale-wise convolution block (SCB) [59] with the residual-in-residual structure and a pixelshuffle layer are adopted to compose our reconstruction (REC) module. The REC module contains  $R$  residual groups for information interaction. Each residual group has three SCBs and a short skip connection. The output feature of  $R$  residual groups is upsampled by a pixelshuffle layer to obtain the final HR residual frame  $\hat{I}_t$ .

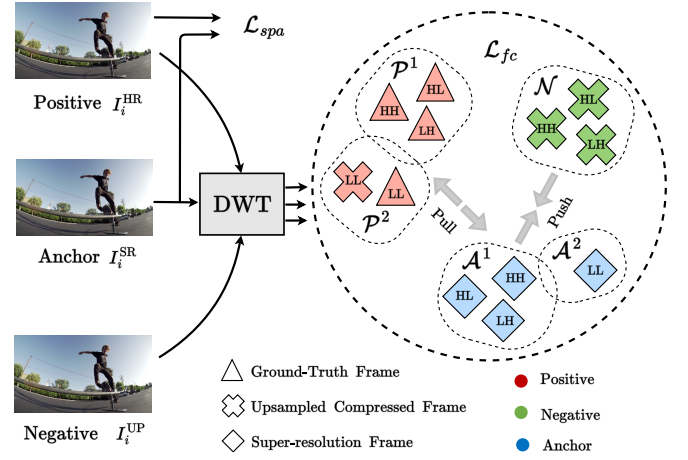


Fig. 6. The loss functions used for training the FCVSR model.

### D. Loss Functions

The proposed model is optimized using the overall loss function  $\mathcal{L}_{all}$  given below:

$$\mathcal{L}_{all} = \mathcal{L}_{spa} + \alpha \mathcal{L}_{fc}, \quad (14)$$

where  $\alpha$  is the weight factor,  $\mathcal{L}_{spa}$ ,  $\mathcal{L}_{fc}$  are the spatial loss, frequency-aware contrastive loss, respectively, and their definition are provided below.

1) *Spatial Loss*: The Charbonnier loss function [52] is adopted as our spatial loss function for supervising the generation of SR results in the spatial domain:

$$\mathcal{L}_{spa} = \sqrt{\|I_t^{HR} - I_t^{SR}\|^2 + \epsilon^2}, \quad (15)$$

in which  $I_t^{HR}$  is the uncompressed HR frame and the penalty factor  $\epsilon$  is set to  $1 \times 10^{-4}$ .

2) *Frequency-aware Contrastive Loss*: The frequency-aware contrastive loss is designed based on the 2D discrete wavelet transform (DWT) to differentiate positive samples and negative samples. Given a training group with a bilinearly upsampled compressed image  $I_i^{UP}$ , the corresponding uncompressed HR image  $I_i^{HR}$  and the restored SR image  $I_i^{SR}$ , 2D-DWT decomposes each of them into four frequency subbands: LL, HL, LH and HH. Two positive sets are defined as  $\mathcal{P}_i^1 = \{I_i^{HR(HH)}, I_i^{HR(HL)}, I_i^{HR(LH)}\}$  and  $\mathcal{P}_i^2 = \{I_i^{HR(LL)}, I_i^{UP(LL)}\}$ , while one negative set is denoted as  $\mathcal{N}_i = \{I_i^{UP(HH)}, I_i^{UP(HL)}, I_i^{UP(LH)}\}$ . Two anchor sets  $\mathcal{A}_i^1 = \{I_i^{SR(HH)}, I_i^{SR(HL)}, I_i^{SR(LH)}\}$ ,  $\mathcal{A}_i^2 = \{I_i^{SR(LL)}\}$  are constructed. Based on these definitions, two frequency-aware contrastive losses for the  $i$ -th train group are:

$$\mathcal{L}_i^1 = -\frac{1}{G_p^1} \sum_{l=1}^{G_p^1} \log \frac{\exp(s(a_l^1, p_l^1)/\tau)}{\exp(s(a_l^1, p_l^1)/\tau) + \sum_{k=1}^{G_g} \exp(s(a_l^1, g_k)/\tau)}, \quad (16)$$

$$\mathcal{L}_i^2 = -\frac{1}{G_p^2} \sum_{l=1}^{G_p^2} \log \frac{\exp(s(a^2, p_l^2)/\tau)}{\exp(s(a^2, p_l^2)/\tau) + \sum_{k=1}^{G_g} \exp(s(a^2, g_k)/\tau)}, \quad (17)$$

TABLE I

QUANTITATIVE COMPARISON IN TERMS OF PSNR (dB), SSIM AND VMAF ON THREE PUBLIC TESTING DATASETS UNDER LDB CONFIGURATION. THE FLOPS IS CALCULATED ON LR VIDEO FRAME WITH  $64 \times 64$  RESOLUTION AND FPS IS CALCULATED ON REDS4 DATASET. THE BEST AND THE SECOND-BEST RESULTS ARE HIGHLIGHTED AND UNDERLINED.

Datasets	Methods	Param. ↓ FLOPs ↓ FPS↑			QP = 22			QP = 27			QP = 32			QP = 37		
		(M)	(G)	(1/s)	PSNR↑ / SSIM↑ / VMAF↑	PSNR↑ / SSIM↑ / VMAF↑	PSNR↑ / SSIM↑ / VMAF↑	PSNR↑ / SSIM↑ / VMAF↑	PSNR↑ / SSIM↑ / VMAF↑	PSNR↑ / SSIM↑ / VMAF↑	PSNR↑ / SSIM↑ / VMAF↑	PSNR↑ / SSIM↑ / VMAF↑				
CVCP [30]	EDVR-L [16]	20.69	354.07	2.02	31.76 / 0.8629 / 68.23	30.58 / 0.8377 / 56.39	29.07 / 0.8045 / 41.72	27.38 / 0.7670 / 25.53								
	BasicVSR [13]	<u>6.30</u>	367.72	0.85	31.80 / 0.8631 / 76.44	30.46 / 0.8349 / 65.14	29.05 / 0.8031 / 47.06	27.33 / 0.7661 / 29.59								
	IconVSR [13]	8.70	576.45	0.51	31.86 / 0.8637 / 77.94	30.48 / 0.8354 / 64.69	29.10 / 0.8043 / 47.77	27.40 / 0.7678 / 30.05								
	BasicVSR++ [38]	7.32	395.69	0.74	31.89 / 0.8647 / 77.55	30.66 / 0.8388 / 66.43	29.13 / 0.8058 / 50.08	27.43 / 0.7682 / 34.11								
	FTVSR++ [18]	10.80	1148.85	0.27	<u>31.92 / 0.8656 / 78.52</u>	<u>30.69 / 0.8393 / 66.89</u>	<u>29.14 / 0.8063 / 51.96</u>	<u>27.44 / 0.7697 / 35.06</u>								
	FCVSR-S (ours)	<b>3.70</b>	<b>68.82</b>	<b>5.28</b>	31.86 / 0.8650 / 78.27	30.64 / 0.8388 / 65.96	29.10 / 0.8058 / 51.39	<u>27.44 / 0.7700 / 35.07</u>								
	FCVSR (ours)	8.81	<u>165.36</u>	<u>2.39</u>	<b>31.94 / 0.8669 / 78.69</b>	<b>30.70 / 0.8403 / 66.97</b>	<b>29.18 / 0.8077 / 52.03</b>	<b>27.46 / 0.7704 / 35.63</b>								
REDS [60]	EDVR-L [16]	20.69	354.07	2.02	29.05 / 0.7991 / 81.60	27.60 / 0.7470 / 59.90	26.40 / 0.7072 / 46.31	24.87 / 0.6585 / 28.80								
	BasicVSR [13]	<u>6.30</u>	367.72	0.85	29.13 / 0.8005 / 81.13	27.62 / 0.7512 / 63.49	26.43 / 0.7079 / 46.82	24.99 / 0.6603 / 29.49								
	IconVSR [13]	8.70	576.45	0.51	29.17 / 0.8009 / 81.52	27.73 / 0.7519 / 62.91	26.45 / 0.7090 / 47.48	24.99 / 0.6609 / 29.73								
	BasicVSR++ [38]	7.32	395.69	0.74	29.23 / 0.8036 / 81.83	27.79 / 0.7543 / 63.63	26.50 / 0.7098 / 47.78	25.05 / 0.6620 / 31.25								
	FTVSR++ [18]	10.80	1148.85	0.27	<u>29.26 / 0.8029 / 81.58</u>	<u>27.81 / 0.7564 / 65.22</u>	<u>26.53 / 0.7106 / 48.57</u>	<u>25.09 / 0.6625 / 31.81</u>								
	FCVSR-S (ours)	<b>3.70</b>	<b>68.82</b>	<b>5.28</b>	29.14 / 0.8002 / 81.18	27.66 / 0.7505 / 63.14	26.42 / 0.7089 / 47.75	24.93 / 0.6611 / 31.56								
	FCVSR (ours)	8.81	<u>165.36</u>	<u>2.39</u>	<b>29.28 / 0.8039 / 81.87</b>	<b>27.92 / 0.7591 / 65.63</b>	<b>26.64 / 0.7161 / 48.59</b>	<b>25.20 / 0.6694 / 32.05</b>								
Vimeo-90K [57]	EDVR-L [16]	20.69	354.07	2.02	25.27 / 0.7135 / 66.57	24.31 / 0.6586 / 52.82	23.29 / 0.5958 / 34.74	22.09 / 0.5284 / 20.43								
	BasicVSR [13]	<u>6.30</u>	367.72	0.85	25.30 / 0.7155 / 67.23	24.36 / 0.6610 / 52.69	23.34 / 0.5989 / 35.51	22.15 / 0.5314 / 20.52								
	IconVSR [13]	8.70	576.45	0.51	25.46 / 0.7225 / 68.77	24.41 / 0.6638 / 52.88	23.36 / 0.5993 / 35.53	22.16 / 0.5305 / 20.41								
	BasicVSR++ [38]	7.32	395.69	0.74	25.55 / 0.7270 / 70.35	24.43 / 0.6639 / <u>53.93</u>	23.37 / 0.5976 / 35.30	22.18 / 0.5326 / 20.60								
	FTVSR++ [18]	10.80	1148.85	0.27	<u>25.58 / 0.7278 / 70.68</u>	<u>24.44 / 0.6657 / 53.53</u>	23.39 / <u>0.6024</u> / 36.16	<u>22.20 / 0.5338 / 20.90</u>								
	FCVSR-S (ours)	<b>3.70</b>	<b>68.82</b>	<b>5.28</b>	25.35 / 0.7194 / 68.36	24.43 / 0.6647 / 53.50	<u>23.40</u> / 0.6021 / <u>36.25</u>	22.19 / <u>0.5340</u> / <u>21.08</u>								
	FCVSR (ours)	8.81	<u>165.36</u>	<u>2.39</u>	<b>25.61 / 0.7307 / 71.50</b>	<b>24.58 / 0.6707 / 54.79</b>	<b>23.47 / 0.6052 / 37.20</b>	<b>22.25 / 0.5366 / 21.60</b>								

where  $G_p^1$ ,  $G_p^2$  and  $G_g$  are the number of sets  $\mathcal{P}^1$ ,  $\mathcal{P}^2$  and  $\mathcal{N}$ ,  $\tau$  is the temperature parameter and  $s(\cdot, \cdot)$  is the similarity function.  $a$ ,  $p$ , and  $g$  represent the anchor, positive, and negative samples, respectively.

The total frequency-aware contrastive loss is defined as:

$$\mathcal{L}_{fc} = \frac{1}{M_s} \sum_{i=1}^{M_s} (\mathcal{L}_i^1 + \mathcal{L}_i^2), \quad (18)$$

where  $M_s$  is the number of samples.

#### IV. EXPERIMENT AND RESULTS

##### A. Implementation Details

In this work, an FCVSR model and its lightweight model, i.e., FCVSR-S, are proposed for the compressed VSR task. The FCVSR model employs the following hyper parameters and configurations: the number of the adaptive convolutions in the MGAA module is set as  $N = 6$ ; the decomposition number in the MFFR module is set as  $Q = 8$ ; the number of residual groups in the REC module is set as  $R = 10$ . The FCVSR-S model is associated with lower computational complexity. Its number of the adaptive convolutions in the MGAA module is set as  $N = 4$ , the decomposition number of the decoupler is set as  $Q = 4$  in the MFFR module, and the number of residual groups is set as  $R = 3$  in the REC module. These two models all take 7 frames as the model input and use the overall loss function to train them. The weight factor of the overall loss function  $\alpha$  is set to 1. The  $L_1$  distance is adopted

as the similarity function  $s(\cdot)$  and the temperature parameter  $\tau$  is 1 in  $\mathcal{L}_{fc}$ . The compressed frames are cropped into  $128 \times 128$  patches and the batch size is set to 8. Random rotation and reflection operations are adopted to increase the diversity of training data. The proposed models are implemented based on PyTorch and trained by Adam [61]. The learning rate is initially set to  $2 \times 10^{-4}$  and gradually halves at 2K, 8K and 12K epochs. The total number of epochs is 30K. All experiments are conducted on PCs with RTX-3090 GPUs and Intel Xeon(R) Gold 5218 CPUs.

##### B. Experimental Setup

Following the common practice in the previous works [13, 18, 38], our models are trained separately on three public training datasets, CVCP [30], REDS [60] and Vimeo-90K [57], and evaluated their corresponding test sets, CVCP10 [30], REDS4 [60], and Vid4 [57] respectively. The downsampled LR videos are generated using a Bicubic filter with a factor 4. All training and test compressed videos are created using the downsampling-then-encoding procedure and compressed by HEVC HM 16.20 [62] under the Low Delay B mode with four different QP values: 22, 27, 32 and 37.

The peak signal-to-noise ratio (PSNR), structural similarity index (SSIM) [63], and video multi-method assessment fusion (VMAF) [64] are adopted as evaluation metrics for the quantitative benchmark. PSNR and SSIM were widely used to evaluate the quality of videos while VMAF was proposed by Netflix to evaluate the perceptual quality of videos. We also

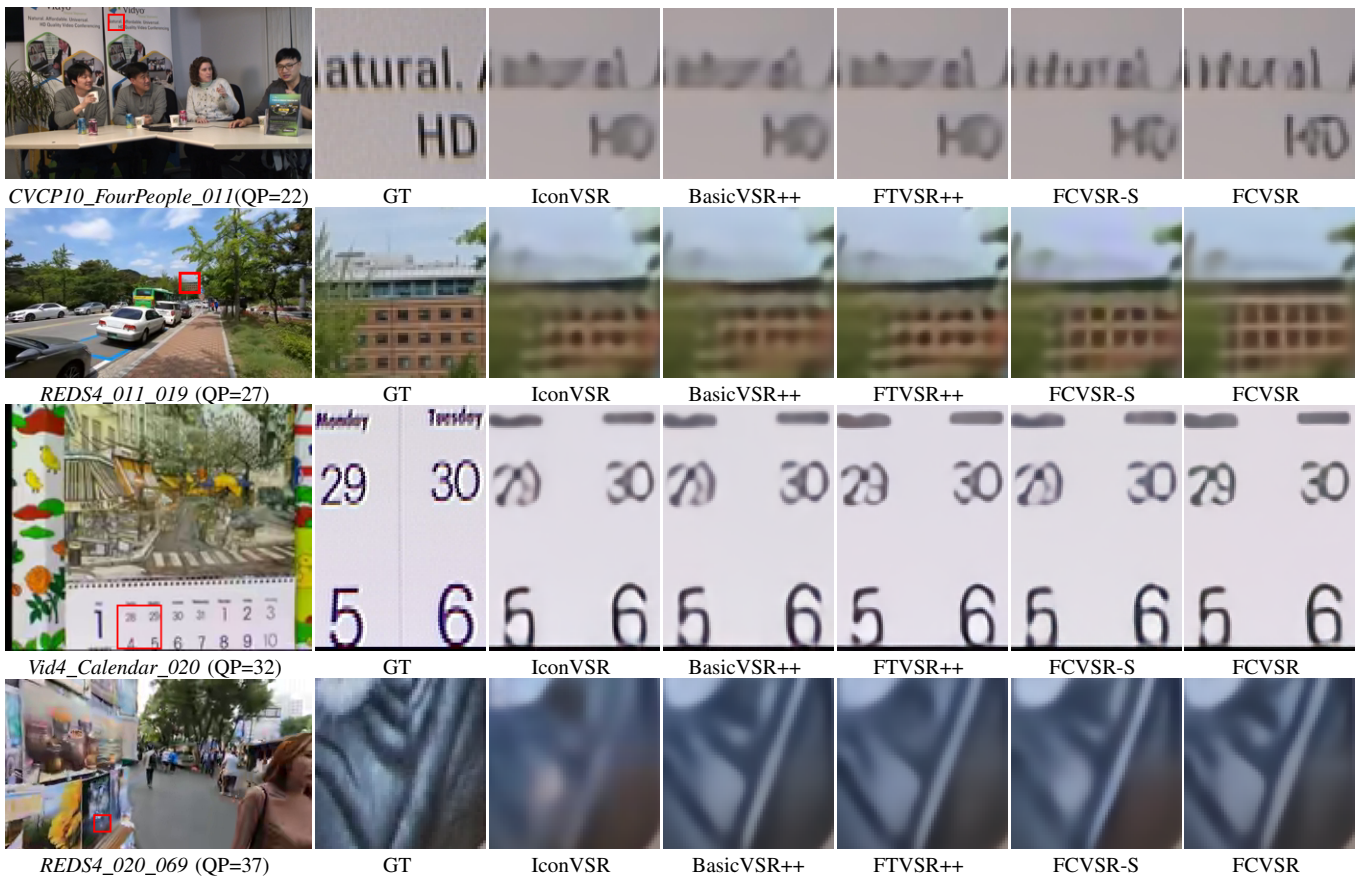


Fig. 7. Visual comparison results between FCVSR models and three benchmark methods.

measured the model complexity in terms of the floating point operations (FLOPs), inference speed (FPS) and the number of model parameters.

Five state-of-the-art methods including EDVR-L [16], BasicVSR [13], IconVSR [13], BasicVSR++ [38] and FTVSR++ [18] are benchmarked against the proposed models. To ensure a fair comparison, we retrained EDVR-L [16], BasicVSR [13], IconVSR [13], BasicVSR++ [38] and FTVSR++ [18] following the same training-evaluation procedure as FCVSR model, using their publicly released source code.

### C. Comparison with State-of-the-Art VSR methods

The quantitative results of our models for three training-test sets are summarized in Table I. It can be observed that our FCVSR model achieves the best super-resolution performance in terms of all three quality metrics and for all QP values, compared with five State-of-the-Art (SoTA) VSR models. The FCVSR-S model also offers second-best results compared to other benchmarks in a few cases.

To comprehensively demonstrate the effectiveness of our models, visual comparison results have been provided in Fig. 7, in which example blocks generated by FCVSR models are compared with those produced by IconVSR, BasicVSR++ and FTVSR++. It is clear in these examples that our results contain fewer artifacts and finer details compared to other benchmarks.

The results of the model complexity comparison in terms of model parameters, FLOPs, and FPS for all the models tested are provided in Table I. Here, inference speed (FPS) is based on the REDS4 dataset. Among all the VSR methods, our FCVSR-S model is associated with the lowest model complexity based on three complexity measurements. The complexity-performance trade-off can also be illustrated by Fig. 1, in which all FCVSR models are all above the Pareto front curve formed by five benchmark methods. This confirms the practicality of the proposed FCVSR models.

### D. Ablation Study

To further verify the effectiveness of the main contributions in this work, we have created different model variants in the ablation study, and used the REDS4 dataset (QP = 37) in this experiment.

We first tested the contribution of the MGAA module (and its sub-blocks) by creating the following variants. (v1.1) w/o MGAA - the MGAA module is removed and the features of frames are fused by a concatenation operation and a convolution layer to obtain the aligned features. We have also tested the effectiveness of the Motion Estimator within the MGAA module, obtaining (v1.2) w/o ME - the input neighboring features are directly fed into the MGAC layer without the guidance of motion offsets to generate the aligned features. The MGAA module has also been replaced by other existing alignment modules including flow-based alignment



TABLE II  
ABLATION STUDY RESULTS FOR THE PROPOSED FCVSR MODEL.

Models	PSNR(dB)↑/SSIM↑/VMAF↑	Param.↓ (M)	FLOPs↓ (G)	FPS↑ (1/s)
(v1.1) w/o MGAA	25.04 / 0.6615 / 30.62	8.25	155.30	3.43
(v1.2) w/o ME	25.12 / 0.6641 / 31.63	8.49	157.91	3.62
(v1.3) Flow(Spynet)	24.83 / 0.6565 / 28.67	6.82	129.29	4.89
(v1.4) Flow(RAFT)	25.07 / 0.6620 / 31.27	10.63	173.74	2.85
(v1.5) DCN	25.01 / 0.6598 / 30.79	8.79	170.84	3.02
(v1.6) FGDA	25.10 / 0.6631 / 31.74	10.45	210.64	2.10
(v2.1) w/o MFFR	25.10 / 0.6630 / 31.45	8.20	159.57	3.02
(v2.2) w/o FBE	25.16 / 0.6668 / 31.95	8.81	165.36	2.68
(v2.3) w/o FFE	25.14 / 0.6664 / 31.92	8.81	165.36	2.76
(v3.1) w/o $\mathcal{L}_{fc}$	25.12 / 0.6652 / 31.85	8.81	165.36	2.39
(v3.2) w/o $\mathcal{L}_i^1$	25.15 / 0.6676 / 31.92	8.81	165.36	2.39
(v3.3) w/o $\mathcal{L}_i^2$	25.17 / 0.6682 / 31.97	8.81	165.36	2.39
<b>FCVSR</b>	<b>25.20 / 0.6694 / 32.05</b>	8.81	165.36	2.39

modules ((v1.3) Spynet [7] and (v1.4) RAFT [8]), deformable convolution-based alignment modules ((v1.5) DCN [10]), and flow-guided deformable alignment module ((v1.6) FGDA [38]) to verify the effectiveness of MGAA module.

The effectiveness of the MFFR module has also been fully evaluated by removing it from the pipe, resulting in (v2.1) w/o MFFR. The contributions of each branch in this module have also been verified by creating (v2.2) w/o FBE - removing the feedback enhancement branch and (v2.3) w/o FFE - disabling the feedforward enhancement branch.

The results of these variants and the full FCVSR model have been summarized in TABLE II. It can be observed that the full FCVSR model is outperformed by all these model variants in terms of three quality metrics, which confirms the contributions of these key models and their sub-blocks.

Finally, to test the contribution of the proposed frequency-aware contrastive loss, we re-trained our FCVSR model separately by removing the  $\mathcal{L}_{fc}$  (v3.1) or its high/low frequency terms,  $\mathcal{L}_i^1$  (v3.2) and  $\mathcal{L}_i^2$  (v3.3), respectively, resulting in three additional variants as shown in Table II. It can be observed that the proposed frequency-aware contrastive loss (and its high/low frequency sub losses) does consistently contribute to the final performance according to the results.

## V. CONCLUSION

In this paper, we proposed a frequency-aware video super-resolution network, FCVSR, for compressed video content, which consists of a new motion-guided adaptive alignment (MGAA) module for improved feature alignment and a novel multi-frequency feature refinement (MFFR) module that enhances the fine detail recovery. A frequency-aware contrastive loss is also designed for training the proposed framework with optimal super resolution performance. We have conducted a comprehensive comparison experiment and ablation study to evaluate the performance of the proposed method and its primary contributions, and the results show up to a 0.14dB PSNR gain over the SoTA methods. Due to its superior performance and relatively low computational complexity, we believe this work makes a strong contribution to the research

field of video super resolution, and is suitable for various application scenarios.

## REFERENCES

- [1] W. Zheng, H. Xu, P. Li, R. Wang, and X. Shao, "Sac-rsm: A high-performance uav-side road surveillance model based on super-resolution assisted learning," *IEEE Internet of Things Journal*, 2024.
- [2] M. Farooq, M. N. Dailey, A. Mahmood, J. Moonrinta, and M. Ekpanyapong, "Human face super-resolution on poor quality surveillance video footage," *Neural Computing and Applications*, vol. 33, pp. 13 505–13 523, 2021.
- [3] Z. Chen, L. Yang, J.-H. Lai, and X. Xie, "Cunerf: Cube-based neural radiance field for zero-shot medical image arbitrary-scale super resolution," in *Proceedings of the IEEE/CVF International Conference on Computer Vision*, 2023, pp. 21 185–21 195.
- [4] Z. Qiu, Y. Hu, X. Chen, D. Zeng, Q. Hu, and J. Liu, "Rethinking dual-stream super-resolution semantic learning in medical image segmentation," *IEEE Transactions on Pattern Analysis and Machine Intelligence*, 2023.
- [5] J.-H. Kang, M. S. Ali, H.-W. Jeong, C.-K. Choi, Y. Kim, S. Y. Jeong, S.-H. Bae, and H. Y. Kim, "A super-resolution-based feature map compression for machine-oriented video coding," *IEEE Access*, vol. 11, pp. 34 198–34 209, 2023.
- [6] C. Lin, Y. Li, J. Li, K. Zhang, and L. Zhang, "Luma-only resampling-based video coding with cnn-based super resolution," in *2023 IEEE International Conference on Visual Communications and Image Processing*, 2023, pp. 1–5.
- [7] A. Ranjan and M. J. Black, "Optical flow estimation using a spatial pyramid network," in *Proceedings of the IEEE Conference on Computer Vision and Pattern Recognition*, 2017, pp. 4161–4170.
- [8] Z. Teed and J. Deng, "Raft: Recurrent all-pairs field transforms for optical flow," in *Proceedings of the European Conference on Computer Vision*, 2020, pp. 402–419.
- [9] J. Dai, H. Qi, Y. Xiong, Y. Li, G. Zhang, H. Hu, and Y. Wei, "Deformable convolutional networks," in *Proceedings of the IEEE International Conference on Computer Vision*, 2017, pp. 764–773.
- [10] X. Zhu, H. Hu, S. Lin, and J. Dai, "Deformable convnets v2: More deformable, better results," in *Proceedings of the IEEE/CVF Conference on Computer Vision and Pattern Recognition*, 2019, pp. 9308–9316.
- [11] A. Arnab, M. Dehghani, G. Heigold, C. Sun, M. Lučić, and C. Schmid, "Vivit: A video vision transformer," in *Proceedings of the IEEE/CVF International Conference on Computer Vision*, 2021, pp. 6836–6846.
- [12] J. Ho, T. Salimans, A. Gritsenko, W. Chan, M. Norouzi, and D. J. Fleet, "Video diffusion models," *Advances in Neural Information Processing Systems*, vol. 35, pp. 8633–8646, 2022.
- [13] K. C. Chan, X. Wang, K. Yu, C. Dong, and C. C. Loy, "Basicvsr: The search for essential components in video super-resolution and beyond," in *Proceedings of the IEEE/CVF Conference on Computer Vision and Pattern Recognition*, 2021, pp. 4947–4956.
- [14] M. Liu, S. Jin, C. Yao, C. Lin, and Y. Zhao, "Temporal consistency learning of inter-frames for video super-resolution," *IEEE Transactions on Circuits and Systems for Video Technology*, vol. 33, no. 4, pp. 1507–1520, 2022.
- [15] Y. Tian, Y. Zhang, Y. Fu, and C. Xu, "Tdan: Temporally-deformable alignment network for video super-resolution," in *Proceedings of the IEEE/CVF Conference on Computer Vision and Pattern Recognition*, 2020, pp. 3360–3369.
- [16] X. Wang, K. C. Chan, K. Yu, C. Dong, and C. Change Loy, "Edvr: Video restoration with enhanced deformable convolutional networks," in *Proceedings of the IEEE/CVF Conference on Computer Vision and Pattern Recognition Workshops*, 2019, pp. 1954–1963.

- [17] C. Liu, H. Yang, J. Fu, and X. Qian, "Learning trajectory-aware transformer for video super-resolution," in *Proceedings of the IEEE/CVF Conference on Computer Vision and Pattern Recognition*, 2022, pp. 5687–5696.
- [18] Z. Qiu, H. Yang, J. Fu, D. Liu, C. Xu, and D. Fu, "Learning degradation-robust spatiotemporal frequency-transformer for video super-resolution," *IEEE Transactions on Pattern Analysis and Machine Intelligence*, pp. 14 888–14 904, 2023.
- [19] S. Zhou, P. Yang, J. Wang, Y. Luo, and C. C. Loy, "Upscale-a-video: Temporal-consistent diffusion model for real-world video super-resolution," in *Proceedings of the IEEE/CVF Conference on Computer Vision and Pattern Recognition*, 2024, pp. 2535–2545.
- [20] X. Yang, C. He, J. Ma, and L. Zhang, "Motion-guided latent diffusion for temporally consistent real-world video super-resolution," in *European Conference on Computer Vision*. Springer, 2025, pp. 224–242.
- [21] M. Afonso, F. Zhang, and D. R. Bull, "Video compression based on spatio-temporal resolution adaptation," *IEEE Transactions on Circuits and Systems for Video Technology*, vol. 29, no. 1, pp. 275–280, 2018.
- [22] M. Shen, P. Xue, and C. Wang, "Down-sampling based video coding using super-resolution technique," *IEEE Transactions on Circuits and Systems for Video Technology*, vol. 21, no. 6, pp. 755–765, 2011.
- [23] M. Khani, V. Sivaraman, and M. Alizadeh, "Efficient video compression via content-adaptive super-resolution," in *Proceedings of the IEEE/CVF International Conference on Computer Vision*, 2021, pp. 4521–4530.
- [24] J. Yang, C. Yang, F. Xiong, F. Wang, and R. Wang, "Learned low bitrate video compression with space-time super-resolution," in *Proceedings of the IEEE/CVF Conference on Computer Vision and Pattern Recognition*, 2022, pp. 1786–1790.
- [25] D. Bull and F. Zhang, *Intelligent image and video compression: communicating pictures*. Academic Press, 2021.
- [26] Q. Ding, L. Shen, L. Yu, H. Yang, and M. Xu, "Blind quality enhancement for compressed video," *IEEE Transactions on Multimedia*, pp. 5782–5794, 2023.
- [27] N. Jiang, W. Chen, J. Lin, T. Zhao, and C.-W. Lin, "Video compression artifacts removal with spatial-temporal attention-guided enhancement," *IEEE Transactions on Multimedia*, pp. 5657–5669, 2023.
- [28] D. Luo, M. Ye, S. Li, C. Zhu, and X. Li, "Spatio-temporal detail information retrieval for compressed video quality enhancement," *IEEE Transactions on Multimedia*, vol. 25, pp. 6808–6820, 2022.
- [29] Y. Li, P. Jin, F. Yang, C. Liu, M.-H. Yang, and P. Milanfar, "Comisr: Compression-informed video super-resolution," in *Proceedings of the IEEE/CVF International Conference on Computer Vision*, 2021, pp. 2543–2552.
- [30] P. Chen, W. Yang, M. Wang, L. Sun, K. Hu, and S. Wang, "Compressed domain deep video super-resolution," *IEEE Transactions on Image Processing*, vol. 30, pp. 7156–7169, 2021.
- [31] H. Zhang, X. Zou, J. Guo, Y. Yan, R. Xie, and L. Song, "A codec information assisted framework for efficient compressed video super-resolution," in *European Conference on Computer Vision*, 2022, pp. 220–235.
- [32] Y. Wang, T. Isobe, X. Jia, X. Tao, H. Lu, and Y.-W. Tai, "Compression-aware video super-resolution," in *Proceedings of the IEEE/CVF Conference on Computer Vision and Pattern Recognition*, 2023, pp. 2012–2021.
- [33] Q. Zhu, F. Chen, Y. Liu, S. Zhu, and B. Zeng, "Deep compressed video super-resolution with guidance of coding priors," *IEEE Transactions on Broadcasting*, 2024.
- [34] G. He, S. Wu, S. Pei, L. Xu, C. Wu, K. Xu, and Y. Li, "Fmvsr: Feature multiplexing video super-resolution for compressed video," *IEEE Access*, vol. 9, pp. 88 060–88 068, 2021.
- [35] M. V. Conde, Z. Lei, W. Li, C. Bampis, I. Katsavounidis, and R. Timofte, "Aim 2024 challenge on efficient video super-resolution for av1 compressed content," *arXiv preprint arXiv:2409.17256*, 2024.
- [36] L. Chen, "Gaussian mask guided attention for compressed video super resolution," in *IEEE 2023 20th International Computer Conference on Wavelet Active Media Technology and Information Processing*, 2023, pp. 1–6.
- [37] Z. Qiu, H. Yang, J. Fu, and D. Fu, "Learning spatiotemporal frequency-transformer for compressed video super-resolution," in *European Conference on Computer Vision*. Springer, 2022, pp. 257–273.
- [38] K. C. Chan, S. Zhou, X. Xu, and C. C. Loy, "Basicvsr++: Improving video super-resolution with enhanced propagation and alignment," in *Proceedings of the IEEE/CVF Conference on Computer Vision and Pattern Recognition*, 2022, pp. 5972–5981.
- [39] J. Xiao, Z. Lyu, C. Zhang, Y. Ju, C. Shui, and K.-M. Lam, "Towards progressive multi-frequency representation for image warping," in *Proceedings of the IEEE/CVF Conference on Computer Vision and Pattern Recognition*, 2024, pp. 2995–3004.
- [40] F. Li, L. Zhang, Z. Liu, J. Lei, and Z. Li, "Multi-frequency representation enhancement with privilege information for video super-resolution," in *Proceedings of the IEEE/CVF International Conference on Computer Vision*, 2023, pp. 12 814–12 825.
- [41] J. Xiao, X. Jiang, N. Zheng, H. Yang, Y. Yang, Y. Yang, D. Li, and K.-M. Lam, "Online video super-resolution with convolutional kernel bypass grafts," *IEEE Transactions on Multimedia*, vol. 25, pp. 8972–8987, 2023.
- [42] J. Zhu, Q. Zhang, L. Fei, R. Cai, Y. Xie, B. Sheng, and X. Yang, "Fffn: Frame-by-frame feedback fusion network for video super-resolution," *IEEE Transactions on Multimedia*, vol. 25, pp. 6821–6835, 2022.
- [43] A. A. Baniya, T.-K. Lee, P. W. Eklund, and S. Aryal, "Omni-directional video super-resolution using deep learning," *IEEE Transactions on Multimedia*, vol. 26, pp. 540–554, 2023.
- [44] C. Liu and D. Sun, "On bayesian adaptive video super resolution," *IEEE Transactions on Pattern Analysis and Machine Intelligence*, vol. 36, no. 2, pp. 346–360, 2013.
- [45] Z. Xiong, X. Sun, and F. Wu, "Robust web image/video super-resolution," *IEEE Transactions on Image Processing*, vol. 19, no. 8, pp. 2017–2028, 2010.
- [46] Q. Zhu, F. Chen, S. Zhu, Y. Liu, X. Zhou, R. Xiong, and B. Zeng, "Dvsrnet: Deep video super-resolution based on progressive deformable alignment and temporal-sparse enhancement," *IEEE Transactions on Neural Networks and Learning Systems*, 2024.
- [47] T. Qing, X. Ying, Z. Sha, and J. Wu, "Video super-resolution with pyramid flow-guided deformable alignment network," in *IEEE 2023 3rd International Conference on Electrical Engineering and Mechatronics Technology*, 2023, pp. 758–764.
- [48] J. Tang, C. Lu, Z. Liu, J. Li, H. Dai, and Y. Ding, "Ctvsr: Collaborative spatial-temporal transformer for video super-resolution," *IEEE Transactions on Circuits and Systems for Video Technology*, 2023.
- [49] Y. Hu, Z. Chen, and C. Luo, "Lamd: Latent motion diffusion for video generation," *arXiv preprint arXiv:2304.11603*, 2023.
- [50] Z. Chen, F. Long, Z. Qiu, T. Yao, W. Zhou, J. Luo, and T. Mei, "Learning spatial adaptation and temporal coherence in diffusion models for video super-resolution," in *Proceedings of the IEEE/CVF Conference on Computer Vision and Pattern Recognition*, 2024, pp. 9232–9241.
- [51] S. Dong, F. Lu, Z. Wu, and C. Yuan, "Dfvsr: Directional frequency video super-resolution via asymmetric and enhancement alignment network," in *Proceedings of the International Joint Conferences on Artificial Intelligence*, 2023, pp. 681–689.
- [52] W.-S. Lai, J.-B. Huang, N. Ahuja, and M.-H. Yang, "Fast and accurate image super-resolution with deep laplacian pyramid

- networks,” *IEEE Transactions on Pattern Analysis and Machine Intelligence*, vol. 41, no. 11, pp. 2599–2613, 2018.
- [53] D. Fuoli, L. Van Gool, and R. Timofte, “Fourier space losses for efficient perceptual image super-resolution,” in *Proceedings of the IEEE/CVF International Conference on Computer Vision*, 2021, pp. 2360–2369.
- [54] L. Jiang, B. Dai, W. Wu, and C. C. Loy, “Focal frequency loss for image reconstruction and synthesis,” in *Proceedings of the IEEE/CVF International Conference on Computer Vision*, 2021, pp. 13 919–13 929.
- [55] A. Dosovitskiy, P. Fischer, E. Ilg, P. Hausser, C. Hazirbas, V. Golkov, P. Van Der Smagt, D. Cremers, and T. Brox, “Flownet: Learning optical flow with convolutional networks,” in *Proceedings of the IEEE International Conference on Computer Vision*, 2015, pp. 2758–2766.
- [56] E. Ilg, N. Mayer, T. Saikia, M. Keuper, A. Dosovitskiy, and T. Brox, “Flownet 2.0: Evolution of optical flow estimation with deep networks,” in *Proceedings of the IEEE Conference on Computer Vision and Pattern Recognition*, 2017, pp. 2462–2470.
- [57] T. Xue, B. Chen, J. Wu, D. Wei, and W. T. Freeman, “Video enhancement with task-oriented flow,” *International Journal of Computer Vision*, vol. 127, pp. 1106–1125, 2019.
- [58] Y. Zhang, K. Li, K. Li, L. Wang, B. Zhong, and Y. Fu, “Image super-resolution using very deep residual channel attention networks,” in *Proceedings of the European Conference on Computer Vision*, 2018, pp. 286–301.
- [59] Y. Fan, J. Yu, D. Liu, and T. S. Huang, “Scale-wise convolution for image restoration,” in *Proceedings of the AAAI Conference on Artificial Intelligence*, vol. 34, no. 07, 2020, pp. 10 770–10 777.
- [60] S. Nah, S. Baik, S. Hong, G. Moon, S. Son, R. Timofte, and K. Mu Lee, “Ntire 2019 challenge on video deblurring and super-resolution: Dataset and study,” in *Proceedings of the IEEE/CVF Conference on Computer Vision and Pattern Recognition workshops*, 2019, pp. 0–0.
- [61] D. P. Kingma, “Adam: A method for stochastic optimization,” *arXiv preprint arXiv:1412.6980*, 2014.
- [62] E. Peixoto, T. Shanableh, and E. Izquierdo, “H. 264/avc to hev video transcoder based on dynamic thresholding and content modeling,” *IEEE Transactions on Circuits and Systems for Video Technology*, vol. 24, no. 1, pp. 99–112, 2013.
- [63] Z. Wang, A. C. Bovik, H. R. Sheikh, and E. P. Simoncelli, “Image quality assessment: from error visibility to structural similarity,” *IEEE Transactions on Image Processing*, vol. 13, no. 4, pp. 600–612, 2004.
- [64] Z. Li, C. Bampis, J. Novak, A. Aaron, K. Swanson, A. Moorthy, and J. Cock, “Vmaf: The journey continues,” *Netflix Technology Blog*, vol. 25, no. 1, 2018.